Controlled Surface Morphology

Antifouling Properties of Electrospun Polymeric Coatings Induced by Controlled Surface Morphology

*Fabio L. Favrin, Lorenzo Zavagna, Matteo Sestini, Semih Esin, Bahareh Azimi, Massimiliano Labardi, Mario Milazzo, Giuseppe Gallone, Giovanna Batoni, and Serena Danti**

Nosocomial infections affect implanted medical devices and greatly challenge their functional outcomes, becoming sometimes life threatening for the patients. Therefore, aggressive antibiotic therapies are administered, which often require the use of last-resort drugs, if the infection is caused by multi-drug-resistant bacteria. Reducing the risk of bacterial contamination of medical devices in the hospitals has thus become an emerging issue. Promising routes to control these infections are based on materials provided with intrinsic bactericidal properties (i.e., chemical action) and on the design of surface coatings able to limit bacteria adhesion and fouling phenomena (i.e., physical action), thus preventing bacterial biofilm formation. Here, we report the development and validation of coatings made of layer-by-layer deposition of electrospun poly(vinylidene fluoride-*co*-trifluoro ethylene) P(VDF-TrFE) fibers with controlled orientations, which ultimately gave rise to antifouling surfaces. The obtained 10-layer surface morphology with 90° orientation fibers was able to efficiently prevent the adhesion of bacteria, by establishing a superhydrophobic-like behavior compatible with the Cassie-Baxter regimen. Moreover, the results highlighted that surface wettability and bacteria adhesion could be controlled using fibers with diameter comparable to bacteria size (i.e., achievable via electrospinning process), by tuning the intra-fiber spacing, with relevant implications in the future design of biomedical surface coatings.

1. Introduction

In the era of pandemics and multi-drug resistance, the research for new strategies to control infections has become a worldwide priority.[1] In healthcare, nosocomial infections, including surgical and post-surgical complications due to hospital-originating (i.e., nosocomial) bacteria that colonize percutaneous and implanted devices (e.g., catheters, orthopedic endoprostheses, heart valves, stents, and breast implants) involve huge costs, estimated in millions euros in Europe annually.[2] Environmental and skin-resident bacteria can exploit wounds, surgical accesses, and post-surgical draining catheters as passageways to enter the body of patients, and reach inner organs, which are otherwise sterile.[3] Once a site has become infected, antibiotic therapy is required for a complete recovery. In some cases, however, the therapeutic dose of the drug cannot reach the infected area, for example, across an avascular fibrotic scar formed around a non-biodegradable implant, making the antibiotic poorly effective, so that after an initially apparent healing, resistant species take place, leading to microbial reinforcement.[2] In this context, the development of effective antibacterial treatments for surfaces is of utmost importance for the success of many biomaterial-related surgical procedures.[2,3] In this framework, a promising route is based on providing devices with unfavorable surfaces for bacterial adhesion, namely, enabling the surfaces with physical obstacles that hinder the generation of bacterial biofilms and allow the immune system of the host organism, along with antibiotic treatments, to properly perform. Among possible solutions, highly hydrophobic surface coatings have shown capability of preventing biofouling through a physical mechanism, which has been originally observed in nature.[4] For instance, wings of insects like cicada and dragonflies have a nanopatterned surface with high aspect ratio cone-like nanopillars, which is unfavorable for *Pseudomonas aeruginosa* (*P. aeruginosa*) adhesion. It has been speculated that this is the result of an evolutionary adaptation to the environment aimed at preventing the formation of biofilms, as they affect the aerodynamics of such insects.[5–8] Scientists have observed many natural systems that exploit similar strategies, which also enable improvement of dynamic or self-cleaning performances. Therefore, a

---

F. L. Favrin, L. Zavagna, M. Sestini, B. Azimi, Dr. M. Milazzo, Prof. G. Gallone, Prof. S. Danti
Department of Civil and Industrial Engineering, University of Pisa, Largo Lucio Lazzarino 2, 56122, Pisa, Italy
E-mail: serena.danti@unipi.it
Prof. S. Esin, Dr. B. Azimi, Prof. G. Batoni
Department of Translational Research and New Technologies in Medicine and Surgery, University of Pisa, via San Zeno 35-39, 56123, Pisa, Italy
Dr. M. Labardi, Prof. S. Danti
Institute for Chemical and Physical Processes (IPCF), National Research Council (CNR), Pisa Research Area, Via Moruzzi 1, 56124, Pisa, Italy
Dr. M. Milazzo, S. Danti
Department of Civil and Environmental Engineering, Massachusetts Institute of Technology (MIT), Massachusetts Ave. 77, Cambridge, Massachusetts 02139, USA

The ORCID identification number(s) for the author(s) of this article can be found under https://doi.org/10.1002/eem2.12773.

DOI: 10.1002/eem2.12773

highly desired property to limit the biofouling phenomenon is super-hydrophobicity, occurring as a combined effect of hydrophobic materials and surface morphologies under some circumstances.

On a superhydrophobic surface, the water contact angle (WCA) reaches or overcomes 150°. This is greatly superior to 90° WCA, observed in hydrophobic surfaces. In such conditions, the water droplet cannot spread on the surface and keeps a roundish shape, leading to easily roll off the surface, while removing possible contaminants.[9,10] Similar effects have been investigated at different scales to prevent the attachment of cells, micro-, and macro-organisms.[11,12] Natural anti-fouling surfaces exploiting morphological features are found in about 900 marine species of the *Elasmobranchii* family,[13] a group that includes sharks and rays.[14,15] In plants, the self-cleaning mechanisms due to super-hydrophobicity are observed, among others, on lotus and rice leaves. The so-called "lotus effect" avails itself of the leave surface topology, which presents a pattern of shaped cones with nanoscale hair-like structures.[16,17] Understanding the antifouling properties of the biological surfaces has thus become essential to engineer new anti-biofouling solutions.[18,19]

Artificial attempts to shape surfaces with bioinspired antifouling properties have been carried out using lithography and self-assembly techniques.[10,20,21] Some commercial products are designed to mimic shark skin or lotus surface. Interesting examples are made of poly(dimethyl siloxane) and thermoplastic polyurethane (by Sharklet Technologies, Inc.), whose micro-patterned surfaces, based on either sharklet-like or distributed pillar patterns, offer valuable anti-biofouling properties and have resulted effective in preventing bacterial adhesion in skin-related applications.[22,23]

The successful antimicrobial mechanisms of micro- and nano-structured surfaces have been investigated by analyzing specific parameters, such as the distribution density and the shape of the surface features.[24,25] Scientists have shared different opinions in designing effective antimicrobial nano-structured surfaces, but a consensus is still missing so far.[26] As an example, Li et al.[27] found that an increased number of nanopillars per surface unit are beneficial for a significant antifouling effect. This result was confirmed by Kelleher et al.[5] and by Linklater et al.,[28] who assessed the performance of cicada wings and synthetic nanostructures made of silicon, respectively. In contrast, Xue et al.[29] theorized that a low density using sharp nanopillars could be more effective; later, Fisher et al.[30] gave an experimental demonstration using *P. aeruginosa*.

In the last decade, physico-chemical properties of superhydrophobic materials have been investigated due to the relevant implications in industry, environment, and healthcare sectors.[31,32] However, some issues have still to be solved, including technological costs, biocompatibility, and durability of micro- and nano-structured surfaces, which overall require further research to select suitable materials and appropriate fabrication procedures to be implemented in industrial-scale processes.[33]

Electrospinning is one among the most promising nanotechnologies, used to obtain small size fibers and particles, with high potential to be upscaled at an industrial level. Electrospun fibrous meshes in some cases have shown to contribute to reach super-hydrophobicity, because of the resulting texture.[34] Even though electrospinning does not allow a precise spatial control over topology, it is a cheaper and more up-scalable technique than other nanopatterning systems (e.g., etching, photolithography), which instead possess high topology control on small surface areas, and is thus suitable for industrial-scale manufacturing. Among others, a great advantage of electrospinning is the large variety of polymers that can be processed.[35,36] Among others, poly(vinylidene fluoride-*co*-trifluoroethylene) [P(VDF-TrFE)] is a partially fluorinated copolymer, in which the C-F bond enables high chemical stability and piezoelectricity, entitled with a hydrophobic character. Several studies have addressed the effect of the electrospinning process on the crystallinity and piezoelectric properties of P(VDF-TrFE).[37,38] P(VDF-TrFE) fibers showed good cytocompatibility toward epithelial cells.[39] For their enhanced piezoelectric properties, occurring as a consequence of the electrospinning process, currently, electrospun P(VDF-TrFE) fibers have risen a great interest as nanogenerators and nanosensors.[38,40] However, electrospinning, as a manufacturing technique requires the optimization of many process parameters, including voltage, feed rate, viscosity and electrical properties of the solution, set-up geometry, temperature, and humidity, to achieve the desired size, interspace and alignment of fibers, among other specific properties.[41]

Our study exploits electrospinning to fabricate highly hydrophobic textures provided with intrinsic antifouling properties by controlling the geometry of the deposited fibers, to be used as surface coatings. Fiber coatings built up as superimposed layers of aligned ultrafine fibers made of P(VDF-TrFE) were electrospun to obtain different orientations of the alignment direction between consecutive layers. We report on the fabrication and testing of two "generations" of coatings deposited on aluminum and P(VDF-TrFE) surfaces, made of multi-layered aligned ultrafine P(VDF-TrFE) fibers. The morphology of the obtained textured surfaces and the WCAs were investigated to assess a superhydrophobic response. Ultimately, we performed a biological analysis on the capability of the obtained coatings of limiting bacterial adhesion, including *P. aeruginosa* and *E. coli*, as a primary sign of fouling.

Demonstrating industrially affordable coatings, which are antibacterial by sole morphological actions, would greatly contribute to reducing the development of multi-drug-resistant bacteria and the consumption of antibiotics with beneficial effects on health and environment.

2. Results

2.1. Characterization of Fiber Coatings

The produced fiber coatings underwent a morphological characterization, followed by a physico-chemical (including wettability and surface composition) and stability characterizations. First-generation (1G) fiber coatings composed of multi-layered aligned fibers of P(VDF-TrFE) were produced with an electrospinning set-up using an aluminum foil as a substrate. We fabricated different fiber coatings with four layers of aligned fibers (1G–4L) having alternating orientations (0°–45°, 0°–60°, 0°–90°). We report hereafter the results concerning the 0–90° arrangement. The results of other configurations are given in the Supporting Information. The surface morphology of the 1G coatings was studied via Scanning Electronic Microscopy (SEM); coatings made of fibers oriented at 0°–90° are shown in **Figure** 1a,b, whereas coatings made of fibers oriented at 0°–45° and 0°–60° in Figure S1, Supporting Information. The high rotational speed of the collector and the high applied electric potential led to aligned ultrafine fibers. As reported in Figure 1c, P(VDF-TrFE) fibers had a mean diameter value of 0.97 ± 0.34 μm (i.e., size range of 0.32–1.65 μm). The pore size distribution in the fibrous matrix ranged in 1.05–63.88 μm^2, with a pore mean value of 11.60 μm^2 (Figure 1d, black marker) and an average surface porosity of about 58%.

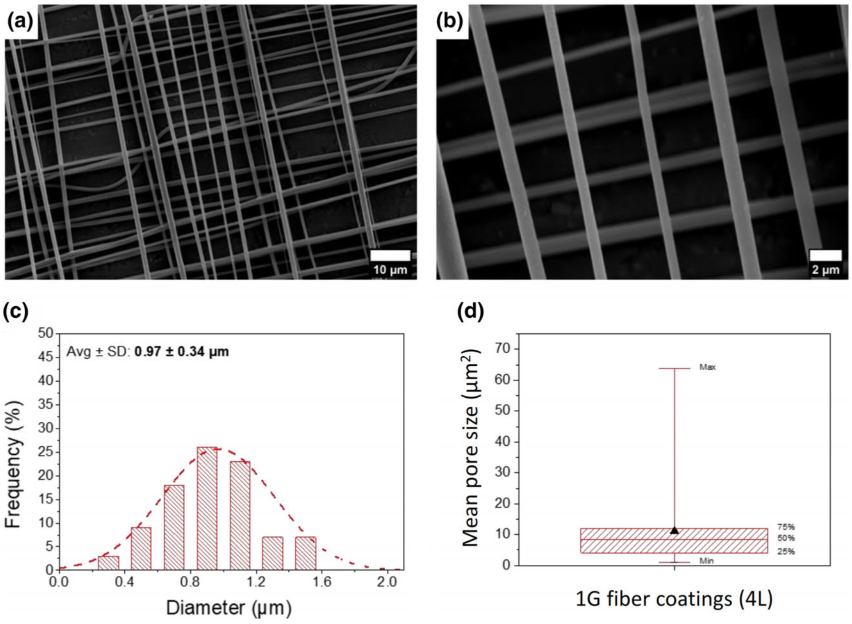

Figure 1. a, b) SEM micrographs of first-generation (1G) fiber coatings made of four layers (4 L). Fibers on a same layer appear aligned and perpendicular with fibers of different layers. a) Voltage 10 kV, 4000× magnification; b) voltage 10 kV, 16 000× magnification. c) Diameter distribution and d) mean pore size whisker plot of the fiber coatings. The ultrafine fibers have a mean diameter of 0.97 ± 0.34 μm (with dashed line as an eye guide) and a mean pore size of 11.6 μm^2 (d, black marker). The pore area values ranged in 1.05–63.88 μm^2 (minimum and maximum value, respectively). The horizontal bar inside the colored block indicates the median pore size of 8.52 μm^2.

Based on the experience and outcomes gained with the 1G fiber coatings, we developed a second-generation (2G) fiber coatings able to assemble additional layers. In the 2G fiber coatings, we increased the electrospinning runtime, and fibers were collected on a P(VDF-TrFE) film instead of on an aluminum foil. With this protocol, we collected up to 10 layers of P(VDF-TrFE) fibers with a 0°–90° arrangement. The presence of the P(VDF-TrFE) film as a substrate and the increased collection time led to firmer samples than those obtained with 1G fiber coatings. Differently from the 1G samples, the fibers of the 2G fiber coatings were well anchored to the substrate without affecting the overall arrangement of the sample.

To study the properties of interest of 1G and 2G samples with those exhibited by plain surfaces of the same material, P(VDF-TrFE) films with thickness of 60 ± 10 μm were produced using the blade coating technique (**Table 1**).

The application of a post-processing thermal treatment (TT) to the film influenced its surface morphology. Figure S2, Supporting Information, shows SEM micrographs of the surfaces of films produced without (Figure S2a, Supporting Information) and with (Figure S2b, Supporting Information) the application of a post-deposition TT. In fact, heating the film after its deposition expedited the solvent evaporation and led to a non-porous surface (Figure S2b, Supporting Information). By contrast, without TTs, a low solvent evaporation rate generated a porous surface (Figure S2a, Supporting Information). These two different morphologies affected the wettability of the surfaces. TT films had a hydrophilic behavior with a WCA equal to 78° ± 1°, whereas films without TTs showed a hydrophobic behavior with WCA equal to 106° ± 2 (Table 1). In view of collecting fiber coatings on a plain homogeneous film, which could better enhance the hydrophobic properties of the fibers, we selected TT P(VDF-TrFE) films as substrates for 2G samples. A complete characterization of the fiber coatings is reported in **Tables 2** and **3**.

Figure 2 displays the micrographs of the 2G coatings produced by collecting 10 layers of P(VDF-TrFE) fibers (2G–10L) on TT P(VDF-TrFE) films and reports the distributions of fiber diameter and pore size.

The dashed line in Figure 2c evinces less variability of the fiber diameters and then the improved reliability of the fabrication method with respect to the 1G samples. P(VDF-TrFE) fibers had a mean diameter of 1.31 ± 0.17 μm (i.e., size range 0.81–1.72 μm). The pore size distribution of the 2G fiber coatings ranged in 1.02–32.95 μm^2 with a mean pore size of 5.22 μm^2 (Figure 2c, black marker), accounting for an average surface porosity of about 22%. A similar analysis was carried out on the 2G fiber coatings with 8 layers (2G–8L). Table 2 includes all the results of 1G and 2G samples along with the main differences between the two electrospinning protocols employed.

In detail, pore size distribution analysis showed a reduction in pore size with increasing generations and fiber layers (Figure S3, Supporting Information). In 2G–10L samples, 65% of pores had size lower than 5 μm^2, whereas 2G–8L and 1G–4L samples had 43% and 35% of pores with size lower than 5 μm^2, respectively.

Table 1. P(VDF-TrFE) film "w/ TT" and "w/o TT" indicates film with and without thermal treatment, respectively.

Sample	Thickness (μm)	WCA (°)
P(VDF-TrFE) film w/ TT	60 ± 10	78 ± 1
P(VDF-TrFE) film w/o TT	60 ± 10	106 ± 2

Table 2. Comparison of first- and second-generation (G) coatings fabricated with different layers (L) of P(VDF-TrFE) fibers, that is, 1G (4 L), 2G (8 L), and 2G (10 L) versus the respective plain substrates without fibers.

Sample	Substrate	Run time for each layer (s)	Fiber diameter (μm)	Mean pore size (μm^2)	Porosity (%)	WCA (°)
1G–4 L	Aluminum	35 ± 5	0.97 ± 0.34	11.60	58	140 ± 2
2G–8 L	P(VDF-TrFE) film w/ TT	45 ± 5	1.20 ± 0.20	10.10	46	122 ± 2
2G–10 L	P(VDF-TrFE) film w/ TT	45 ± 5	1.31 ± 0.17	5.22	22	127 ± 5

In the table are also reported the main differences in the electrospinning process between 1G and 2G fiber coatings.

Table 3. Porosity evaluation following the image analysis presented.

Sample	Number of layers considered	Average pore size (μm^2)	Average fiber–fiber distance (µm)	Measured porosity (MP) (%)	Predicted porosity (PP) (%)
1G–4 L	1	—	9.9	89.7	90.8
	2	97.4	9.9	82.4	82.4
	3	47.0	6.9	76.8	74.9
	4	11.6	3.4	57.8	68.0
2G–8 L	1	—	7.9	78.4	84.9
	2	61.9	7.9	72.2	72.2
	3	26.1	5.1	54.4	61.3
	4	10.1	3.2	45.9	52.1
2G–10 L	1	—	3.4	63.5	66.0
	2	11.5	3.4	43.5	43.5
	3	5.2	2.3	21.8	28.7
	4	[a]	[a]	[a]	18.9

[a] Pores too small to be reliably assessed.

Static WCA measurements were performed to evaluate the wettability of all the fabricated fiber coatings. **Figure 3** shows the data collected for both 1G–4L and 2G–8L and 2G–10L fiber coatings, together with the results of plain P(VDF-TrFE) films, with (w/) and without (w/o) TT.

Significant differences were recognized between the 2G fiber coatings (both 8 L and 10 L) and the plain films with (***$p < 0.001$) and without (**$p < 0.01$) TT. Significant changes were also observed between 1G fiber coatings and TT (**$p < 0.01$) or non-TT (*$p < 0.05$) films, underpinning that the presence of the fiber coatings significantly increased the hydrophobicity of the surface with respect to the plain P(VDF-TrFE) films. Furthermore, it is interesting to note that WCA of 1G fiber coatings was significantly different from that of 2G fiber coatings, whereas WCAs of 2G fiber coatings with different layer numbers (i.e., 8 L and 10 L) were similar, and coincided within the experimental error. This indicates that, although the number of deposited layers can play a specific role in determining the final wettability properties, this only occurred to a defined layer extent.

Fourier transform infrared spectroscopy (FTIR) and X-ray photoelectron spectroscopy (XPS) were used to study the chemistry of the fibrous coating, by considering separately the fibers and film. The FTIR spectra depicting P(VDF-TrFE) components, that is, fibers collected at 4500 revolutions per minute (rpm) (i.e., 1811 *g*) and TT film, are presented in Figure S4, Supporting Information. The band around at 880 cm^{-1} is assigned to C–C stretching vibration. The band around at 1180 cm^{-1} is assigned to $–CF_2$ symmetric stretching modes. The bands at 1287 cm^{-1} and 840 cm^{-1} are mixtures of C–F stretching, C–C stretching, and $–CH_2$ rocking vibrations. A band around 1430 cm^{-1} can be attributed to the bending vibration of the $–CH_2$ groups.[42] Both the fibers and film clearly manifest these characteristic bands. Notably, the spectra exhibited prominent characteristic bands at 846, 884, 1124, 1181, 1285, and 1431 cm^{-1}, which are indicative of the β phase of P(VDF-TrFE).[39] Furthermore, electrospinning was observed to augment the intensity of the crystalline bands associated with the β phase. The values of F(β) (%), calculated according to Equation 1, were 90.44% and 79.41% for P(VDF-TrFE) fibers and film, respectively.

$$F(\beta) = \frac{X_\beta}{X_\beta + X_\alpha} = \frac{A_\beta}{1.26\ A_\beta + A_\alpha} \qquad (1)$$

where A_α and A_β correspond to absorption band intensities at 530 cm^{-1} and 840 cm^{-1} for α and β phases, respectively.

The surface chemistry of the 2G–8L fibrous coating (i.e., fibers deposited on the TT film) was assessed via XPS and compared with that of the plain TT film by considering F, C, and O elements, as reported in Figure S5, Supporting Information. On both samples, the contributions related to aliphatic carbon (C–C and C–H), oxygen-bonded carbon (C–O), carbon bonded to strongly electronegative atoms and fluorinated carbon (C–F) were found, as the peaks are positioned at same binding energy values. However, in the 2G–8L and in the film sample the underlying areas were different. The 2G–8L sample was dominated by the C–F contribution (at 290.8 eV), while for the film sample, the largest contribution was from the aliphatic carbon (at 284.8 eV). The fluorine spectrum, on the other hand, can be fitted with a single component, compatible with C–F and

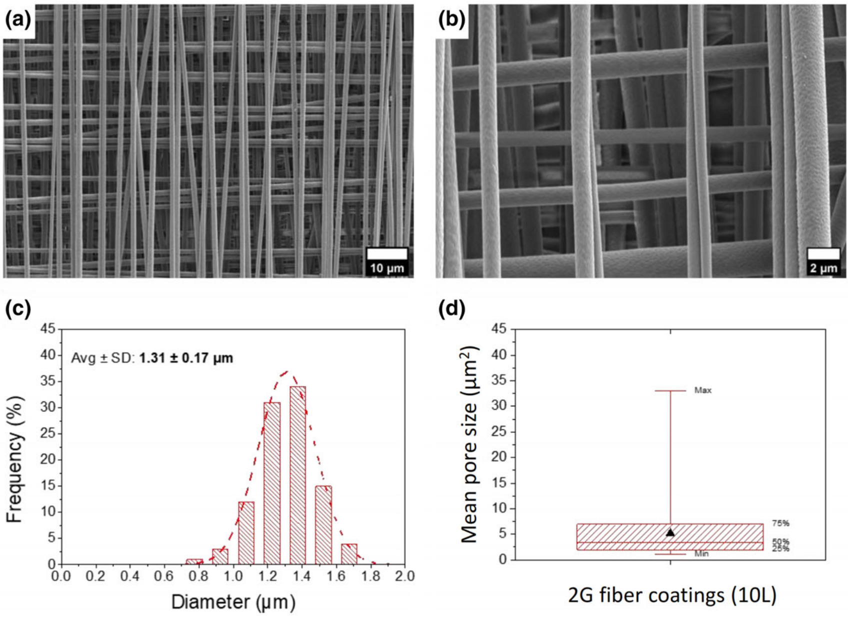

Figure 2. a, b) SEM micrographs, c) diameter distribution, and d) mean pore size whisker plot of second-generation (2G) fiber coatings with 10 layers (10 L) of fibers. The micrographs and the pore size analysis confirmed that 2G fiber coatings have a higher packed structure with respect to 1G ones. a) Voltage 5 kV, 4000× magnification; b) voltage 5 kV, 16 000× magnification. The ultrafine fibers have a mean diameter of 1.31 ± 0.17 µm (with dashed line as an eye guide) and a mean pore value of 5.22 μm^2 (d, black marker). The pore areas values ranged from 1.02 and 32.95 μm^2 (minimum and maximum value, respectively). The horizontal bar inside the colored block indicates the median pore size of 3.38 μm^2.

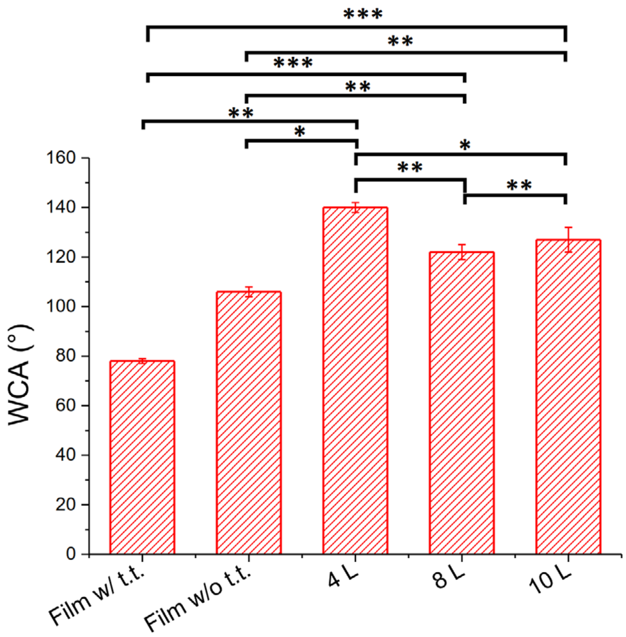

Figure 3. Water contact angle (WCA) measurements. The deposition of fibers significantly increased the hydrophobicity of the surface with respect to the plain films w/ and w/o thermal treatment (t.t.). There are statistically significant differences between 1G and 2G samples series and between the fiber coatings of the same 2G series with 8 layers (8 L) and 10 layers (10 L) of fibers (*$p < 0.05$, **$p < 0.01$, ***$p < 0.001$).

is identical for both samples. The oxygen peak was modest for both samples, and usually imputable to atmospheric contaminations. These results are likely to be attributable to the different techniques used to process P(VDF-TrFE) in the form of fibrous coating and TT film.[37,38]

Finally, the stability of the fibrous coating was investigated from nanomechanical and chemical-morphological point of view by using atomic force microscopy (AFM) and SEM analysis (the latter after applying chemical substances on the samples), respectively.

Mechanical robustness of the produced layered coating was assessed at the single-fiber level by nanomechanical tests performed by AFM in contact mode over the coating surface. Repeated tests demonstrated that fibers typically overcome bending, similarly to a guitar string, with pinning points at a distance of ~50 μm, therefore denoting high robustness, as shown in Video S1, Supporting Information. The pushing force can be calculated as follows.[43] The spring constant k_b pertaining to cantilever buckling (i.e., when the exerted force is along the cantilever axis) is typically much higher than the bending spring constant k (i.e., when the force is along the tip axis). In the present case, it can be derived that $k/k_b = 0.06$. Since $k = 0.2\ \text{N m}^{-1}$, the buckling force is equal to the cantilever deflection Z (nm) measured by the AFM optical lever method multiplied by $k_b = 0.2/0.06 = 3.3\ \text{N m}^{-1}$. Therefore, with reference to Figure S6, Supporting Information, the first fiber was pushed by 1 mN, and the second one by 1.6 mN. Application of a sideway force on the constrained fiber stroke caused its bending, as visible in Video S1, Supporting Information. The elastic force related to such bending is opposed by the elastic force of the cantilever buckling motion, until a maximum force is reached when the probe tip slips off the fiber. Therefore, the fiber stroke behaved like a spring. By measurement of the fiber bending d before slippage, derived from the Video S1, Supporting Information, an effective spring constant value was obtained, which amounted to $F/d = 1\ \text{mN}/5\ \mu\text{m} = 0.2\ \text{N m}^{-1}$. Furthermore, considering the triangular shape of the fiber stroke just before slippage, by a simple geometrical calculation the maximum longitudinal strain of the fiber stroke turned out to be 2%. The Young modulus E was estimated by calculating the tension T along the stretched fiber, which amounted to $T = F/[d/(L/2)]$, where L is the constrained fiber stroke length. The stress s was calculated as T/A, with A the fiber cross section area. In our case, by considering the average fiber diameter $d = 1\ \mu\text{m}$, we obtained $E = 0.35\ \text{GPa}$. The fibers in the orthogonal direction (horizontal direction in Video S2) did not show such large dispacements after similar mechanical stresses. This could be explained by an enhanced immobilization exerted by the overlaid fibers.

Finally, the effect of different chemicals or solutions used for cleaning and disinfecting the surfaces were investigated by determining the stability of the fiber network morphology. Specifically, the 2G–10L samples were treated with a basic solution (i.e., ammonium hydroxide, 25% water solution), an acid solution (i.e., hydrochloric acid water solution 1 N), and an alcohol (i.e., isopropanol). The fibrous coating elicited different wettability to these disinfectants, showing a strongly hydrophobic behavior toward the basic and acid water solutions tested, whereas a complete wettability toward isopropanol. In all cases, the fiber morphology was maintained (Figure S7, Supporting Information). Overall, these outcomes demonstrated a promising nanomechanical and chemical stability of these coatings.

2.2. Bacterial Adhesion on Fiber Coatings

To evaluate the antifouling properties of the samples, we investigated the capability of 0°–90° 1G fiber coatings to reduce *Staphylococcus epidermidis* (*S. epidermidis*) adhesion compared with the uncoated substrate used, namely an aluminum foil. This bacterial species was chosen as is one of the most important commensal microorganisms of the human skin and is often involved in colonization of indwelling medical devices.

SEM micrographs of the 1G samples in contact with *S. epidermidis* are shown in **Figure 4**a,b. The bacteria spread on the last layer of the coating and, in certain areas, through the fiber matrix. To evaluate the antifouling properties, and thus the capability of the coatings to limit the bacterial adhesion, we evaluated the viable bacteria in terms of colony forming units per surface unit (CFU mm^{-2}). The results are reported in Figure 4c. The horizontal bars inside the colored blocks indicate the median values of CFUs, which for uncoated aluminum surface (i.e., black) were 1.34×10^4 CFU mm^{-2}, while for 1G–4L coated aluminum surface (i.e., red) were 0.9×10^4 CFU mm^{-2}. The marker indicates the mean values, that is, in 2.7×10^4 CFU mm^{-2} and 1.3×10^4 CFU mm^{-2} for the uncoated and 1G–4L coated aluminum surfaces, respectively. The presence of the 1G fiber coatings limited bacterial adhesion on the aluminum surface, thus increasing the antifouling properties of the surface. However, a statistically significant difference was not found in terms of *S. epidermidis* viable count in 1G coated and uncoated aluminum.

Subsequently, we developed 2G fiber coatings; to avoid the effect of the substrate material, we used the same material for both the film and the fibrous coating, that is, P(VDF-TrFE). The copolymer underwent a TT in the case of films; thus, we compared their antifouling activity. To better match the dimension of the 2G fibers and pore size, we selected *Escherichia coli* (*E. coli*) to perform the bacterial adhesion assays. SEM micrographs at the endpoint of the assay are presented **Figure 5**a,b.

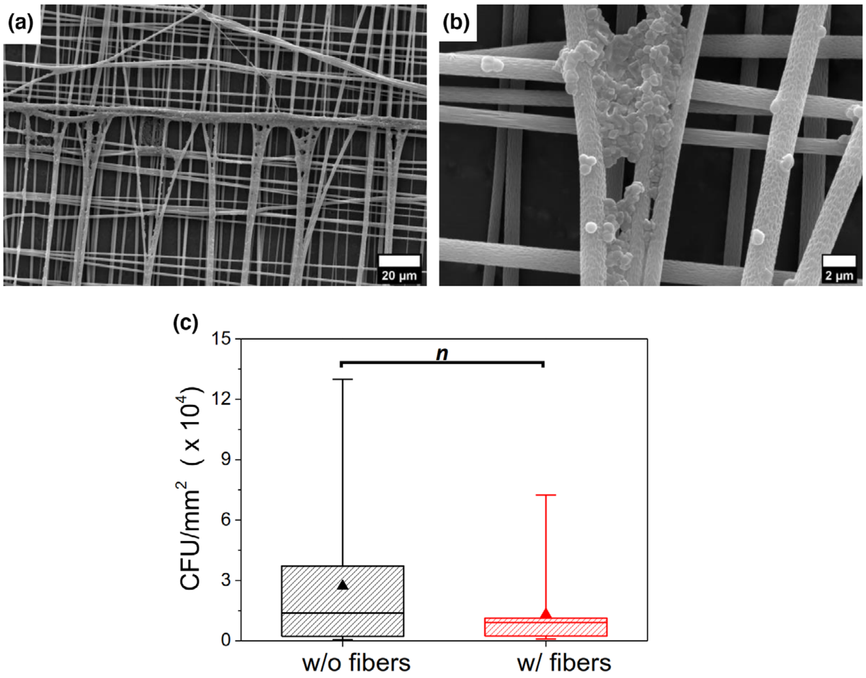

Figure 4. a, b) SEM micrographs of 1G 4-layer (4 L) coatings of P(VDF-TrFE) fibers on an aluminum substrate after exposure to *S. epidermidis*. a) Voltage 5 kV, 4000× magnification; b) Voltage 5 kV, 16 000× magnification. The micrographs suggest that bacteria spread through the fiber coating surface and slightly inside it. c) The whisker plot shows the results of the bacterial adhesion assay between uncoated aluminum films (black) and aluminum films coated with four layers of P(VDF-TrFE) electrospun fibers alternated at 0°–90° orientation, that is, 1G samples (red). *S. epidermidis* was incubated for 4 h at 37 °C. Following incubation, bacteria were washed away and those remaining attached were counted. Triangles indicate the average values in CFU mm^{-2}. Non-significant statistical difference was found between the samples.

Differently from 1G samples, *E. coli* was not able to penetrate the fibrous matrix and adhered only on the top of the coating, particularly where the fibers were in contact with each other. The results reported in Figure 5c suggest that 2G fiber coatings were more effective in limiting bacteria proliferation compared with smooth TT P(VDF-TrFE) films, as also corroborated by SEM micrograph in Figure S3, Supporting Information. The median values, represented by the horizontal bars inside the box, resulted in 4.2×10^4 CFU mm^{-2} for P(VDF-TrFE) film (i.e., black), and in 1.3×10^4 CFU mm^{-2} for 2G–10L coatings (i.e., red). The markers indicate the mean values, namely, 4.3×10^4 CFU mm^{-2} for the P(VDF-TrFE) plain film and 1.7×10^4 CFU mm^{-2} for the 2G–10L fiber coatings. The presence of the fibrous matrix significantly decreased ($p < 0.001$) the adhesion of bacteria. The data collected indicated a reduction in *E. coli* adhesion of approximately 69%. The experiment was repeated using a second Gram-negative bacterium with a size comparable of that of *E. coli*, namely *P. aeruginosa*, which confirmed the previous data (**Figure 6**). In this case, 2G–10L and TT film were also evaluated via confocal laser scanning microscopy (CLSM) after a fluorescent staining with Syto9/propidium iodide, which qualitatively confirmed the decrease in bacteria on the fibrous coating (Figure S9, Supporting Information). Bacterial densities of 14.5 ± 1.5 bacteria/100 μm^2 for films and 6.5 ± 2.9 bacteria/100 μm^2 for 2G–10L surfaces were counted. This result is in line with the decrease evaluated with the CFUs for *E. coli*.

2.3. Antifouling Analysis of Fiber Coatings

We used the Cassie–Baxter (CB) model to comprehend the wettability behavior of the produced surfaces. To understand at which layer, starting from the outermost one, the water would stop infiltrating, we designed an image-based approach by means of both Gimp and ImageJ graphic software (Figure S4, Supporting Information). We aimed at measuring the different possible porosity, underlying a liquid drop on the surface, by assuming different possible penetration levels (see details in the Supporting Information). By using this protocol, we clearly distinguished the porosity underlying the water drop by considering the four outermost layers for all the samples, with the only exception for the 2G fiber coating with 10 layers (10 L), for which the combined four outmost layers led to an almost null porosity (not reported). The values estimated by considering the four outermost layers of the coatings are reported in the column "Measured Porosity" of Table 3. To relate such values with the WCA measurements, we used the CB equation for porous surfaces, reported as Equation 2:

$$\cos(\theta_{\mathrm{CB}}) = \varphi\,[1 + \cos(\theta_{\mathrm{flat}})] - 1 \qquad (2)$$

in which θ_{CB} is the CB equilibrium WCA for a porous surface, φ is the solid fraction of the sample in contact with the water drop (i.e., the ratio of the liquid/solid contact area under the droplet to the total projected area of the drop basement), and θ_{flat} is the WCA in the case of a flat surface of the same material.[44] In our calculations, we used the measured WCA of the non-porous film: $\theta_{\mathrm{flat}} = 78°$. The values of θ_{CB} calculated by using the measured porosity for φ in the previous equation were reported and compared with the WCA angles coming from direct measurements. The data suggested a correlation between the experimental WCA and the θ_{CB} values. For the 10 L sample, the experimental WCA was in good agreement with the θ_{CB} calculated by considering only the first layer of fibers. For the sample with 8 L, the WCA was compatible with the θ_{CB} obtained by considering the three uppermost layers of fibers. Similarly, the WCA measured for the 1G fiber coatings with 4 L was related with the θ_{CB} obtained by considering the first two layers of fibers (**Figure 7**). Finally, we validated our results by estimating the possible porosity via a statistical model. The calculated values are reported in Table 3, column "predicted porosity (PP)."

3. Discussion

The design of coatings able to promote an appropriate interaction with external substances, such as biofluids and living cells, has been revealed crucial for the success of many materials employed in the bioengineering field. Water-repellent and superhydrophobic surfaces have been

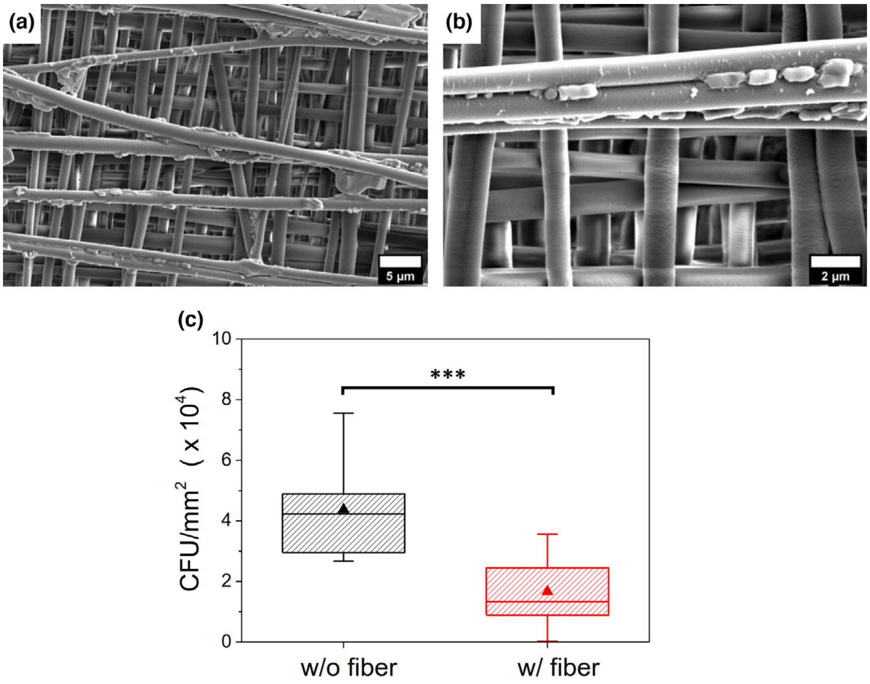

Figure 5. a, b) SEM micrographs of *E. coli* colonies on 2G–10L coating of ultrafine P(VDF-TrFE) fibers. b) Bacteria neither spread throughout the fiber coated surface, nor in its depth. Instead, the adhesion occurred only in the upper layer of fibers and bacteria exhibited a preferential adhesion where fibers were not enough spaced. a) Voltage 5 kV, 8000× magnification; b) voltage 5 kV, 24 000× magnification. c) The graph presents the results of the bacterial adhesion assay considering thermally treated (TT) P(VDF-TrFE) films uncoated (black) and coated (red) with 10 layers (10 L) of P(VDF-TrFE) electrospun fibers alternated at 0°–90° orientation (i.e., 2G–10L fiber coated samples). *E. coli* was incubated for 4 h at 37°C. Following incubation, non-adhered bacteria were washed away and the bacteria that remained attached were counted. Triangles indicate the average values in CFU mm^{-2}. A significant difference is detected between the two samples (***$p < 0.001$).

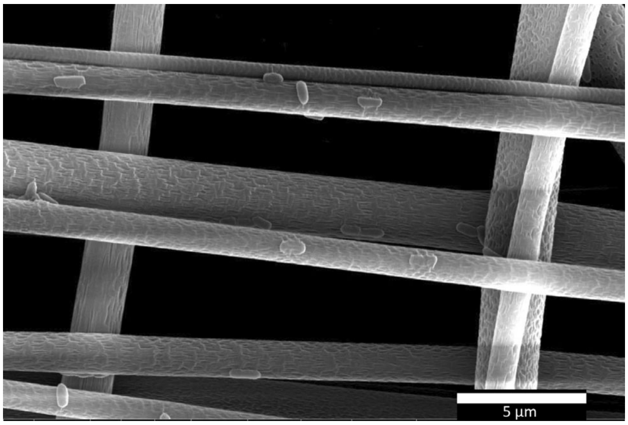

Figure 6. SEM micrograph of *P. aeruginosa* on 2G–10L coating of ultrafine P(VDF-TrFE) fibers alternated at 0°–90° orientation, after incubation for 4 h at 37°C. Before imaging, non-adhered bacteria were washed away. Voltage 15 kV, 16 000× magnification.

observed in nature and have been studied to identify efficient surface topologies to be emulated by engineered materials.[45,46] The literature evinces that surface wettability by aqueous solution (i.e., including protein solution) is strongly reduced on hydrophobic surfaces, namely, with a static contact angle >90°. However, this simple classification using Young's theory,[47] in which only the chemistry of the surface is considered in terms of surface free energy, does not take into consideration the morphology of the surface, assumed to be ideally flat and uniform.

The models that are typically recalled to describe the wettability phenomenon on a rough surface are Wenzel's[48] and by Cassie & Baxter's,[44] which include the effects of the surface conformation. They highlighted how the roughness of the material plays a key factor for the wettability property and clarify that the WCA is not only a function of the surface chemistry and of the static or dynamic regimen, but is also a function of the surface morphology, thus being affected by the surface roughness.[44,48]

Following these studies, other works have outlined that a static WCA greater than 120° gives rise to highly hydrophobic properties, whereas super-hydrophobicity needs to overcome a static WCA of 150°.[33,34,49] However, it has already been demonstrated that such a classification is oversimplified and does not match some experimental studies,[50] in which a superhydrophobic behavior was also evidenced for static contact angles lower than 150°. In view of this, we managed to tailor the wettability of a substrate in TT P(VDF-TrFE) from hydrophilic to superhydrophobic by superimposing an electrospun multi-layered fibers. First, we assessed the feasibility of this hypothesis, by collecting up to four layers (4 L) of aligned fibers with alternate orientations (0°–45°, 0°–60°, 0°–90°) on an aluminum substrate, referred as 1G fiber coatings. Although electrospinning is usually employed to fabricate randomly oriented fiber coatings, the "n-layer-step" procedure, developed within this study, allowed us to deposit layers with different orientations in a simple and effective manner. By applying a considerable voltage and rotational speed (i.e., 35 kV, 1811 cg), we produced uniform, porous, bead-free aligned fibers, as confirmed by SEM micrographs. The WCA measurements corroborated that we successfully fabricated superhydrophobic coatings, and the results of the bacterial assay suggested that the coatings were able to reduce the bacteria adhesion with respect to non-decorated surfaces. However, none statistically significant difference was found in the bacteria limitation using 1G coated aluminum. The reliability of the biological assessment was influenced by different factors. 1G samples were very delicate and easy to tear due to the small amount (four layers) of collected fibers that were also not properly anchored to the aluminum substrate. To improve the fiber adhesion to the substrate and avoid the possible interference played by the different material properties of fibers and substrate, we developed the 2G coatings, consisting of 8 and 10 layers of ultrafine P(VDF-TrFE) fibers electrospun onto a P(VDF-TrFE) film, with each layer made of fibers aligned perpendicularly to the underlying layer. As shown by the SEM micrographs, we collected uniform fibers with larger diameters than those obtained in 1G fiber coatings. The different size between the 1G and 2G fibers can occur due to

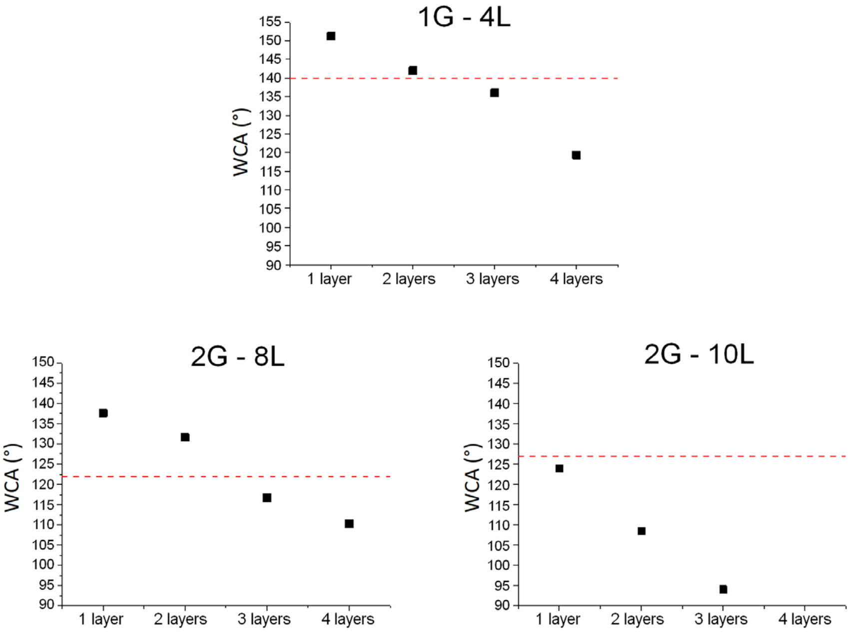

Figure 7. Water contact angle (WCA) values from the Cassie–Baxter (CB) model considering different number of fiber layers for all the samples. The filled black squares indicate the CB contact angle values calculated by using the porosity measured at one, two, three, or four layers. The dashed red lines display the experimental WCA values.

the influence played by the substrate material, acting as a collector in the electrospinning process. The measured WCA confirmed a superhydrophobic behavior, and the antifouling assay proved a statistically significant reduction, up to 69%, of the bacteria adhesion on the 2G fiber coatings with respect to a plain film of P(VDF-TrFE).

These outcomes disclosed the influence of the surface morphology on the resulting antifouling properties. We used the CB model to understand the wettability behavior of the produced surfaces. To this purpose, the effective porosity observed when the drop is in contact with the surface, which concur to determine the penetration of the liquid into the fiber coating, is crucial.

The results for the biological assay of 2G–10L fiber coatings, performed using larger size bacteria than those used for the 1G samples, namely *E. coli* (~1 μm length) was used instead of *S. epidermidis* (~0.5 μm size). The bacterium choice was performed to better match the fiber size of the 2G fiber coatings, thus hampering bacterial spreading on single-fiber surface. In addition, we aimed at having pore size that would prevent bacteria to colonize the substrate film. By interrupting via a three-dimensional (3D) porous surface the bacterial continuity with a size comparable to bacterial size, the adhesion of bacterial aggregates and possibly subsequent biofilm formation can be prevented. The obtained findings showed that bacteria did not penetrate inside underlying fiber layers. On the other hand, concerning 1G samples the SEM micrographs suggested that bacteria could infiltrate the layers, thus revealing an insufficient shielding of the underlying surface. In fact, the data indicated a limitation, yet not statistically significant, in bacterial adhesion, between decorated and undecorated surfaces. The produced 2G fiber coatings demonstrated sufficient mechanical stability on the nanoscale and were compatible with acidic, alkaline and alcoholic disinfectants, which denotes interesting possibility for application in the biomedical field.[2] The possible variability of pore dimensions and local fiber density could be responsible for water and bacteria penetration to some extent. Differently, in 2G fiber coatings, the penetrating water can be stopped by a "cage" of pores small enough to trap it.

To understand at which layer, starting from the outermost one, the water would stop infiltrating, we designed an image-based approach by means of both Gimp and ImageJ graphic software. We used CB equation for porous surfaces to relate such values with the WCA measurements.[44] These observations suggested that the drop fell in CB regimen at different layers for each sample. Concerning the 10 L samples, the results indicated that the drop entered the CB regimen at the first layer of fibers, while for the 8 L samples this phenomenon occurred in the second or third layer of fibers, and for the 4 L samples in the second layer. Such findings were confirmed by SEM images of the bacteria, in which for the 10 L samples the presence of bacteria was observed for the outermost layer, while for the 4 L samples the bacteria penetrated deeper into the fiber structure.

The estimation of the porosity is usually carried out by using image-based methods.[51,52] However, such an approach could become inaccurate in case of multi-layered fiber coatings since raw data are extracted by 2D snapshots. Starting from the traditional approach, we validated our results by estimating the possible porosity via a statistical model. However, when considering more than four layers, we did not achieve reliable results since the assumption of layer independence is not reliable if the area of the fiber superposition becomes unneglectable.

The good agreement between the measured porosity values and the assumed power law values indicated that the assumption of consequent electrospun layers independence could be taken as generally valid for the considered layers; therefore, it could be used for preliminary porosity estimation when characterizing fiber structures. Since we did not consider the surface of fiber superposition sites, the model slightly overestimates the considered porosity, especially for sample with higher fiber density, hence, with more fiber superpositions.

Finally, based on the evaluations made for the measured porosity, we estimated another crucial factor for entering the CB regimen, namely the average fiber distances.[44] Average fiber spacing lengths were obtained as square root of the corresponding average pore sizes. By comparing the experimental WCAs with the expected ones, calculated from the measured porosity, we assessed at which depth the water was averagely stopped in the considered sample. For example, in the case of the 10 L sample, the water never entered the first layer due to very low fiber distances. On the contrary, on the 8 L sample, the water appeared to enter at least two layers of fibers, then, between the 2nd and 3rd layers, the fiber spacing became small enough to reach the CB regimen. The same happened for the 4 L sample, in which water also statistically stopped between the 2nd and 3rd layers. It is therefore reasonable to recognize a superior fiber spacing limit of 6–7 μm, namely only below this limit the penetrating water can enter the CB regimen.

Notably, these findings imply that with a proper choice of both materials and processing parameters, it should be possible to fabricate by electrospun coatings with improved anti-biofouling properties made up of just a couple of layers.

4. Conclusions

In this study, we reported the production of electrospun multi-layered P(VDF-TrFE) fiber coatings with antifouling properties driven by the obtained morphology of the surface. In particular, we firstly assessed the feasibility of this hypothesis by fabricating up to four superimposed layers of oriented fibers, each layer with an alternate orientation with respect to the underlying one, on an aluminum substrate. Thereafter, we optimized the fiber coating by adding up to 10 layers of P(VDF-TrFE) electrospun fibers deposited on a P(VDF-TrFE) film as a substrate. The deposited fibers resulted to averagely have a micrometric size diameter using both substrates, which is in line with bacteria size (e.g., *E. coli*, *P. aeruginosa*). WCA measurements demonstrated that the presence of the fibrous layers raised the hydrophobicity of the surfaces up to the level expected from a CB regimen. This property is considered the main factor responsible for improving the antifouling properties exhibited by fibrous coatings. In fact, antibacterial adhesion assay with the *E. coli* bacteria model, indicated that the presence of the 10 L fibrous coating reduced the bacteria adhesion by approximately 69% with respect to flat P(VDF-TrFE) films. A coherent finding was found using *P. aeruginosa*, which has a size similar with that of *E. coli*. SEM images of bacterial adhesion assays confirmed that the bacteria did not spread in-depth through the fiber layers and that the adhesion occurred only in the outermost layers. Finally, to fully comprehend the experimental results, we proposed an imaging procedure and a statistical model to estimate the porosity of the coatings, which established a superior limit for the fiber spacing, below which the wettability can be described by the CB regimen. These findings pave the way for future evaluations of the wettability and porosity in electrospun fiber coatings and can be used to fabricate tailored surfaces capable to tune water penetration and impede biofilm formation. Such physical-based mechanisms for limiting surface colonization by bacteria disclose remarkable opportunities in healthcare.

5. Experimental Section

Materials: To fabricate the fiber coatings and films, P(VDF-TrFE) powder 70:30 mol.% was purchased from Piezotech Arkema (Pierre-Benite, France). Methyl ethyl ketone (MEK), *Pseudomonas aeruginosa (P. aeruginosa;* PAO1 strain), and electron microscopy-grade 50% glutaraldehyde solution were obtained from Merck KGaA (Darmstadt, Germany). Ammonium hydroxide (25% solution), Tryptone soy broth (TSB), tryptone soy agar (TSA), phosphate-buffered saline (PBS), and saline solution were supplied by Sigma Aldrich (Milan, Italy). Hydrochloric acid (37% solution) and isopropanol were purchased from Carlo Erba (Milan, Italy). All the chemicals are analysis grade. *Escherichia coli* (*E. coli*) (25922), and *Staphylococcus epidermidis* (*S. epidermidis*) (35984) were supplied by American Type Culture Collection (ATCC). Fluoromount-G™ and Syto9/Propidium Iodide, (Filmtracer™ LIVE/DEAD™ viability kit) were supplied by Invitrogen (Fisher Scientific Italia, Segrate, Italy).

Fabrication of P(VDF-TrFE) ultra-aligned fibers: To prepare the electrospinning polymer solution, a 20% w/v (referred to the total solution volume) of P(VDF-TrFE) powder was dissolved in MEK at room temperature (RT). The solution was then left under magnetic stirring for about 12 h until it appeared transparent and homogeneous.

A 1.0 mL plastic syringe fitted with a blunt-tip stainless steel needle (21G × 3/4″) was loaded with a total of 0.7–0.8 mL polymer solution and placed into a syringe pump (NE-300, New Era Pump Systems, Inc., NY, USA). The syringe pump was part of an electrospinning apparatus composed of an 8 cm diameter cylindrical collector and a high-voltage supply unit (S1600079 Linari High Voltage), both from Linari Engineering s.r.l., Pisa, Italy. The needle of the syringe was oriented orthogonally to the cylinder axis, with its tip distant 12 cm from the collector surface. The ground terminal of the high-voltage generator was connected to the metal needle of the syringe, while the positive terminal was connected to the cylindrical collector. The electrospinning process was carried out under 35 kV potential difference, with a flow rate of 0.016 mL min^{-1} from the syringe pump and at a collector rotational speed of 4500 rpm. The set-up and the procedure used are outlined in **Figure 8**.

All the fabrication steps were performed at RT and keeping the relative humidity (RH) at about 40%. To fabricate more complex structures, a "n-layer-step" procedure was used. The method consisted in rotating the sample by a specific angle (i.e., 45°, 60°, or 90°) after spinning each layer. Using this procedure, it was possible to fabricate differently textured structures with different fiber orientations.

The 1G fiber coatings were manufactured by spinning each layer for 30–40 s on an aluminum substrate. A total of four layers with different orientations were collected. The 2G fiber coatings were fabricated by electrospinning each layer for 40–50 s on a P(VDF-TrFE) film, thus finally collecting 8 or 10 layers.

Fabrication of P(VDF-TrFE) films: P(VDF-TrFE) plain films used as substrates for the electrospinning process of 2G samples were prepared by blade coating technique. The glass base table was previously covered with a stretched aluminum foil, and ≈2 mL of PES were poured in front of the moving blade. The gap between the blade and the substrate was set at 700 μm, and the blade was displaced with a velocity of 7 mm s^{-1} to spread the solution on the substrate and form a ≈4 cm × 4 cm P(VDF-TrFE) film. Thereafter the film was either left to rest and dry at RT, or thermally treated (TT). TT films were kept at 70 °C for 30 min and then at 130 °C for 2 h, to fully evaporate the solvent and to promote crystallization; thereafter they were left to cool in the oven down to 60 °C before any further use.

Morphological characterization: Morphological analysis of the fibers was performed via SEM imaging (FEI-FEG-Quanta 450 instrument; Field Electron and Ion Company, Hillsboro, OR, USA). Samples were sputter-coated with a nano-layer of platinum before the analysis. Scans were performed at different magnifications. Image analysis was performed with the ImageJ software (Version 1.53e from

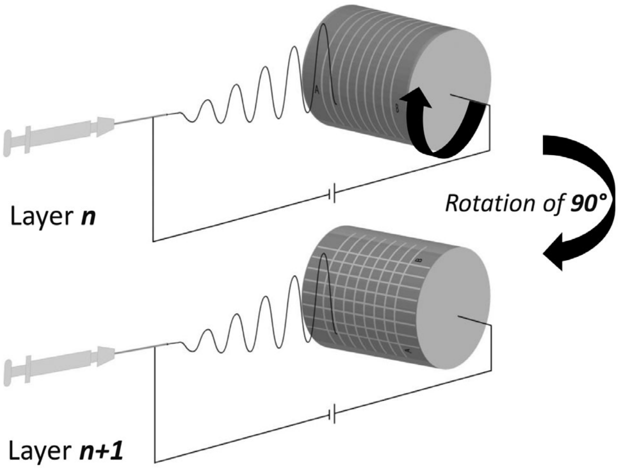

Figure 8. Electrospinning set-up used for the fabrication of 1G and 2G samples and *n-layer-step* procedure. The set-up consisted of a syringe (used on a syringe pump), a rotating collector and a high-voltage generator. After collecting a *n*th layer of fibers for 30–50 s, the substrate is rotated by a specific angle (0°–90° in this figure) and then another layer is deposited (layer $n + 1$).

https://imagej.nih.gov/) and Gimp software (Version 2.10.28), which was used to analyze the pores and estimate the average diameter of 100 fibers per sample. When evaluating the pore sizes, the respective areas were examined by considering their apertures at various depth levels. The morphology of the fibers and the structure of the layers made possible to resolve all four layers for the 1G fiber coatings. On the contrary, concerning the 2G fiber coatings, it was possible to unambiguously differentiate the pores only down to the third layer from the top due to the high fiber density. More information about the image analysis of the pores can be found in the Supporting Information. Pore size were distributed in 5 μm^2 classes by assuming square-like pores and a dimension of interest, that is, $\sqrt{5}$, of the same order of the bacteria size.

In addition to the image analysis of the pores, we double checked the validity of the results by using a statistical model. From a statistical standpoint, the porosity can be regarded as the probability of finding a hole by randomly selecting a pixel inside the region of interest of the treated images. By assuming that the arrangement (i.e., spacing) and the occupation (i.e., dimension) of the fibers in the various layers are almost random and independent, the probability of finding a hole penetrating the two outermost layers will be the product of the porosity of these two layers taken separately. By increasing the number of layers being considered, we expected to find a power law for which the probability of finding a hole deep down to the third layer will be the product of the individual porosities of the first three layers taken separately, and so on.

If we also assume that for each sample the deposited layers are statistically equivalent in terms of fiber densities, we can estimate the porosities at the n^{th} layer as the n-power of the first one. In this respect, we started from the porosity of the two outermost layers, which are most easily and reliably measurable and account for a statistically relevant number of fibers and pores (i.e., $n > 20$). Therefore, the first-layer porosity is estimated as the square root of the two layers porosity and by increasing the number of considered layers, the probability/porosity of the third layer is obtained as the third power of the first-layer porosity, and the fourth layer one as its fourth power.

Wettability of films and fiber coatings: WCA measurements on both 1G and 2G fiber coatings and the plain films used as substrates, were performed by using the sessile drop method in air with a tensiometer (Ramé-hart, model # 100–00230). Drops of ≈15 μL of deionized water were placed on the sample surface, and data were acquired 10 s after the contact between the drop and the sample. Three different points on the sample surface were analyzed for each specimen, and three independent samples were considered. Height profiles of three different films were evaluated at their center using a thickness gauge (Mitutoyo # 7305).

Chemical analysis: The relative fraction of β phase in the copolymer matrix, F(β), was determined by FTIR spectroscopy. The FTIR spectra of the samples were recorded with a Perkin Elmer Spectrum GX spectrometer using a polarized wire grid (Perkin Elmer, Waltham, Massachusetts, USA). The beam, directed orthogonally to the wider specimen surface, was polarized alternatively parallel or orthogonal to the main axis of the fiber. In the case of anisotropic meshes as obtained using the rotating collector, this measurement allows the evaluation of the influence of collector velocity on the P(VDF-TrFE) crystalline phase content of the samples. All the spectra were collected in the mid-IR region (500–1500 cm^{-1}) using 16 scans. The relative fraction of β phase was calculated as from Equation 1.

XPS measurements were performed using a non-monochromated Mg-Ka X-ray source (1254.6 eV) and a VSW HAC 5000 hemispherical electron energy analyzer. Photoelectron spectra were acquired in the constant-pass-energy mode at $E_{pas} = 22$ eV, and the overall energy resolution was 1.2 eV measured as a full width at half maximum (FWHM) of the Ag $3d_{5/2}$ line of a pure silver reference. Pressure during the experiment was kept below 1×10^{-8} Torr. The spectra energy scale was corrected using the C 1 s peak of organic atmospheric contaminants. The recorded spectra were fitted using XPSPeak 4.1 software employing Gauss–Lorentz curves to fit the data after subtraction of a Shirley-type background.

Mechanical and chemical stability analyses: Nanomechanical investigations were performed by a Veeco Instruments Multimode AFM with Nanoscope IIIa controller, operated in contact mode. NanoWorld Arrow-cont silicon cantilevers were used, with 0.2 $N\,m^{-1}$ spring constant, 450 μm length, 45 μm width, 2 μm thickness, and 15 mm tip height. The buckling spring constant was determined according to Grafstrom et al.[43] The probe was scanned in contact mode over 2G–10L coating surface. Fibers comprising the outermost layer could be intercepted, while the ones of the lower layers could not, due to the limited height range of our AFM scanner (∼5 μm). Scans of 10–15 μm size were performed, to strike more than one fiber along the probe trajectory. The AFM cantilever with pointed tip at its edge is oriented along the horizontal axis (Figure S6a, Supporting Information). Fibers of the outermost layer appear as dark lines in the vertical direction. The red light visible around the probe tip comes from the laser used for the optical lever force detection of the AFM.

To test the effect of three different disinfectant solutions on 2G–10L coatings. Isopropanol and ammonium hydroxide (pH 11.8) were used as received. A 1 N HCl solution (pH 0.16) was prepared by dilution in distilled water. For each solution tested, a 70 μL drop was placed on 8 mm × 8 mm sample and let dry under ventilated hood. An untreated sample was observed as control. Samples were then sputter-coated and observed by SEM.

Bacterial adhesion assays: The ability of electrospun fiber coatings to inhibit bacteria adhesion was assessed by evaluating the viable count of either *S. epidermidis* (on 1G fiber coatings) or *E. coli* and *S. aeruginosa* (on 2G fiber coatings). Considering the 1G fiber coatings: three square pieces of aluminum substrates 15 mm × 15 mm (225 mm^2) without fibers and four samples with P(VDF-TrFE) fibers were examined. Similarly, for the 2G fiber coatings three 15 mm × 15 mm (225 mm^2) square pieces of P(VDF-TrFE) films without fibers, and four samples with 10-layer P(VDF-TrFE) fibers were examined. All samples were preliminarily sterilized by exposing each side to UV light for 30 min under a laminar flow hood. Bacterial strains were left to grow overnight (approximately 16 h) at 37 °C, in shaking conditions in 5 mL of bacteriological liquid medium (TSB). Bacterial density was estimated by spectrophotometric measurement of the optical density at 570 nm (OD_{570}) and adjusted to obtain a cell density of approximately 1×10^8 CFU mL^{-1}. Sterile substrates were placed in 90-mm Petri dishes, and a total of 250 μL bacterial suspension in saline solution containing 1% TSB, were poured onto each sample. The plates were then incubated at 37 °C for 4 h. After the treatment, the bacteria suspension was discarded, and the samples were washed three times with 300 μL saline solution to remove non-adherent cells. Thereafter, each sample was immersed in 10 ml of saline solution, briefly shaken and sonicated for 5 min. After sonication and a further 2 min vigorous shaking, up to 10^{-4} serial dilutions were prepared in saline solution and 10 μL of each dilution was plated on TSA in quadruplicates. After further 24 h incubation at 37 °C, viable bacterial colonies formed on the surface were counted and reported as CFU mm^{-2}. For *P. aeruginosa*, a live/dead assay was additionally tested. After washings, the samples, namely P(VDF-TrFE) 2G–10L and TT film, were stained with 200 μL working solution of fluorescence stains SYTO 9 and propidium iodide and incubated for 30 min at RT. The samples were then washed twice with 250 μL of sterile distilled water (dH_2O) and fixed with 250 μL glutaraldehyde (2.5% in dH_2O) for 2 h at RT. The glutaraldehyde was removed, and the samples were washed three times with 250 μL PBS. Finally, the fixed samples were placed over glass slides and covered with 300 μL of mounting media (Fluoromount-G™). Samples were observed on the confocal laser scanning microscope (CLSM) Zeiss LSM 900 Airyscan 2 (Carl Zeiss S.p.A., Milano, Italy). Images were treated and analyzed with Fiji (ImageJ, version 1.54f). For each sample (i.e., w/o and w/fiber coating), the total amount of bacteria was counted for three images (25 μm × 25 μm size) taken in different zones of the sample and normalized per 100 μm^2 surface area. Data are reported as mean and standard deviation of the three measurements.

Statistical analysis: The statistical analysis was carried out using the Jamovi software (Version 1.6.23, https://www.jamovi.org) to specify the significant level of different parameters. Data were analyzed using Mann–Whitney *U* test and choosing p-values < 0.05 as statistically significant. Unless otherwise noted, data are expressed as mean ± standard deviation.

Acknowledgements

F.L.F., L.Z., M.S. contributed equally to this work. The authors thank Dr. Stefano Linari (Linari Engineering s.r.l., Pisa) for the use of electrospinning equipment. The Centre for Instrumentation Sharing of University of Pisa (CISUP) is acknowledged for SEM and CLSM analyses. S.D. greatly thanks Prof. Stefano Caporali (University of Florence, Italy) and Prof. Ranieri Bizzarri (University of Pisa) for their technical contribution to XPS and CSLM analyses, respectively.

Conflict of interest

All the authors declare no conflicts of interest.

Supporting Information

Supporting Information is available from the Wiley Online Library or from the author.

Keywords

additive manufacturing, *Escherichia coli*, fibers, Poly(vinylidene fluoride-co-trifluoro ethylene) P(VDF-TrFE), *Pseudomonas aeruginosa*, superhydrophobic

Received: July 13, 2023
Revised: February 20, 2024
Published online: April 20, 2024

---

[1] P. S. Stewart, T. Bjarnsholt, *Clin. Microbiol. Infect.* **2020**, *26*, 1034.
[2] M. Milazzo, G. Gallone, E. Marcello, M. D. Mariniello, L. Bruschini, I. Roy, S. Danti, *J. Funct. Biomater.* **2020**, *11*, 60.
[3] R. Saginur, K. N. Suh, *Int. J. Antimicrob. Agents* **2008**, *32*, S21.
[4] N. Lin, P. Berton, C. Moraes, R. D. Rogers, N. Tufenkji, *Adv. Colloid Interface Sci.* **2018**, *252*, 55.
[5] S. M. Kelleher, O. Habimana, J. Lawler, B. O'reilly, S. Daniels, E. Casey, A. Cowley, *ACS Appl. Mater. Interfaces* **2016**, *8*, 14966.
[6] C. D. Bandara, S. Singh, I. O. Afara, A. Wolff, T. Tesfamichael, K. Ostrikov, A. Oloyede, *ACS Appl. Mater. Interfaces* **2017**, *9*, 6746.
[7] E. P. Ivanova, J. Hasan, H. K. Webb, V. K. Truong, G. S. Watson, J. A. Watson, V. A. Baulin, S. Pogodin, J. Y. Wang, M. J. Tobin, C. Löbbe, R. J. Crawford, *Small* **2012**, *8*, 2489.
[8] D. E. Mainwaring, S. H. Nguyen, H. Webb, T. Jakubov, M. Tobin, R. N. Lamb, A. H.-F. Wu, R. Marchant, R. J. Crawford, E. P. Ivanova, *Nanoscale* **2016**, *8*, 6527.
[9] G. D. Bixler, B. Bhushan, *Philos. Trans. R. Soc. A Math. Phys. Eng. Sci.* **2012**, *370*, 2381.
[10] S. Nishimoto, B. Bhushan, *RSC Adv.* **2013**, *3*, 671.
[11] M. Salta, J. A. Wharton, P. Stoodley, S. P. Dennington, L. R. Goodes, S. Werwinski, U. Mart, R. J. K. Wood, K. R. Stokes, *Philos. Trans. R. Soc. A Math. Phys. Eng. Sci.* **2010**, *368*, 4729.
[12] L. Hoipkemeier-Wilson, J. F. Schumacher, M. L. Carman, A. L. Gibson, A. W. Feinberg, M. E. Callow, J. A. Finlay, J. A. Callow, A. B. Brennan, *Biofouling* **2004**, *20*, 53.
[13] Q. Bone, R. Moore, *Biology of fishes*, Taylor & Francis Group, New York, NY, USA **2008**.
[14] W. Raschi, C. Tabit, *Mar. Freshw. Res.* **1992**, *43*, 123.
[15] A. W. Lang, P. Motta, P. Hidalgo, M. Westcott, *Bioinspir. Biomim.* **2008**, *3*, 46005.
[16] S. T. Reddy, K. K. Chung, C. J. McDaniel, R. O. Darouiche, J. Landman, A. B. Brennan, *J. Endourol.* **2011**, *25*, 1547.
[17] K. Koch, W. Barthlott, *Philos. Trans. R. Soc. A Math. Phys. Eng. Sci.* **2009**, *367*, 1487.
[18] G. D. Bixler, B. Bhushan, *Soft Matter* **2012**, *8*, 11271.
[19] C. M. Kirschner, A. B. Brennan, *Annu. Rev. Mat. Res.* **2012**, *42*, 211.
[20] G. D. Bixler, A. Theiss, B. Bhushan, S. C. Lee, *J. Colloid Interface Sci.* **2014**, *419*, 114.
[21] N. S. Murthy, R. D. Prabhu, J. J. Martin, L. Zhou, R. L. Headrick, *J. Appl. Phys.* **2006**, *100*, 23538.
[22] E. E. Mann, D. Manna, M. R. Mettetal, R. M. May, E. M. Dannemiller, K. K. Chung, A. B. Brennan, S. T. Reddy, *Antimicrob. Resist. Infect. Control* **2014**, *3*, 28.
[23] A. C. Lima, J. F. Mano, *Nanomedicine* **2015**, *10*, 271.
[24] L. Bocquet, E. Lauga, *Nat. Mater.* **2011**, *10*, 334.
[25] B. Bhushan, Y. C. Jung, K. Koch, *Philos. Trans. R. Soc. A Math. Phys. Eng. Sci.* **2009**, *367*, 1631.
[26] T. E. Catley, R. M. Corrigan, A. J. Parnell, *ACS Omega* **2023**, *8*, 14873.
[27] X. Li, *Phys. Chem. Chem. Phys.* **2016**, *18*, 1311.
[28] D. P. Linklater, H. K. D. Nguyen, C. M. Bhadra, S. Juodkazis, E. P. Ivanova, *Nanotechnology* **2017**, *28*, 245301.
[29] F. Xue, J. Liu, L. Guo, L. Zhang, Q. Li, *J. Theor. Biol.* **2015**, *385*, DOI: 10.1016/j.jtbi.2015.08.011.
[30] L. E. Fisher, Y. Yang, M.-F. Yuen, W. Zhang, A. H. Nobbs, B. Su, *Biointerphases* **2016**, *11*, 11014.
[31] V. K. Manivasagam, G. Perumal, H. S. Arora, K. C. Popat, *J. Biomed. Mater. Res. Part A* **2022**, *110*, 1314.
[32] A. Jaggessar, H. Shahali, A. Mathew, P. K. D. V. Yarlagadda, *J. Nanobiotechnol.* **2017**, *15*, 64.
[33] J. T. Simpson, S. R. Hunter, T. Aytug, *Rep. Prog. Phys.* **2015**, *78*, 86501.
[34] N. Nuraje, W. S. Khan, Y. Lei, M. Ceylan, R. Asmatulu, *J. Mater. Chem. A* **2013**, *1*, 1929.
[35] Y. Muge Sahin, M. Yetmez, F. N. Oktar, O. Gunduz, S. Agathopoulos, E. Andronescu, D. Ficai, M. Sonmez, A. Ficai, *Curr. Med. Chem.* **2014**, *21*, 3391.
[36] W. Serrano-Garcia, I. Cruz-Maya, A. Melendez-Zambrana, I. Ramos-Colon, N. J. Pinto, S. W. Thomas, V. Guarino, *Materials (Basel)* **2023**, *16*, 3106.
[37] W. Zhang, B. Zaarour, L. Zhu, C. Huang, B. Xu, X. Jin, *J. Eng. Fiber. Fabr.* **2020**, *15*, DOI: 10.1177/1558925020939290.
[38] Y. M. Yousry, K. Yao, S. Chen, W. H. Liew, S. Ramakrishna, *Adv. Electron. Mater.* **2018**, 1700562.
[39] B. Azimi, M. S. Sorayani Bafqi, A. Fusco, C. Ricci, G. Gallone, R. Bagherzadeh, G. Donnarumma, M. J. Uddin, M. Latifi, A. Lazzeri, S. Danti, *Tissue Eng. Part A* **2020**, *26*, 1312.
[40] N. Turdakyn, Z. Bekezhankyzy, S. Araby, R. Montazami, Z. Bakenov, G. Kalimuldina, *Energy Rep.* **2023**, *10*, 628.
[41] M. Pourbafrani, S. Azimi, N. Yaghoobi Nia, M. Zendehdel, M. M. Abolhasani, *Exp. Simul. Study* **2023**, *16*, 37.
[42] P. Nallasamy, S. Mohan, *Indian J. Pure Appl. Phys.* **2005**, *43*, 821.
[43] S. Grafstrom, M. Neitzert, T. Hagen, J. Ackermann, R. Neumann, O. Probst, M. Wortge, *Nanotechnology* **1993**, *4*, 143.
[44] A. B. D. Cassie, S. Baxter, *Trans. Faraday Soc.* **1944**, *40*, 546.
[45] W. Barthlott, C. Neinhuis, *Planta* **1997**, *202*, DOI: 10.1007/s004250050096.
[46] C. Neinhuis, W. Barthlott, *Ann. Bot.* **1997**, *79*, 667.
[47] T. Young, *Philos. Trans. R. Soc. Lond. A* **1805**, *95*, 65.
[48] R. N. Wenzel, *Ind. Eng. Chem.* **1936**, *28*, 988.
[49] E. J. Falde, S. T. Yohe, Y. L. Colson, M. W. Grinstaff, *Biomaterials* **2016**, *104*, 87.
[50] R. Vasudevan, A. J. Kennedy, M. Merritt, F. H. Crocker, R. H. Baney, *Colloids Surf. B Biointerfaces* **2014**, *117*, 225.
[51] G. Lo Re, F. Lopresti, G. Petrucci, R. Scaffaro, *Micron* **2015**, *76*, 37.
[52] D. Jenkins, K. Salhadar, G. Ashby, A. Mishra, J. Cheshire, F. Beltran, M. Grunlan, S. Andrieux, C. Stubenrauch, E. Cosgriff-Hernandez, *Bioact. Mater.* **2022**, *13*, DOI: 10.1016/j.bioactmat.2021.11.006.